Analyse of structural and electrical properties of NaBa((2-x))Nd-2x/3Nb5O15 solid solution with (0 < x

M. Belarbi, Manal Benyoussef, Y. Tamraoui, B. Manoun, A. Cantaluppi, D. Favry, K. Taibi, M. El Marssi, A. Lahmar

Analyse of structural and electrical properties of $NaBa_{(2-x)}Nd_{2x/3}Nb_5O_{15}$ solid solution with ($0 \leq x \leq 1$)

M. Belarbi[a,b], M. Benyoussef[a], Y. Tamraoui[c], B. Manoun[c, d], A. Cantaluppi[a], D. Favry[a], K. Taibi[e], M. El Marssi[a], A. Lahmar[a, *]

[a]*Laboratoire de Physique de la Matière condensée (LPMC), 33 Rue saint Leu, 80039 Amiens.*

[b]*Laboratoire de Génie Physique (LGP), Faculté des sciences de la Matière, Université Ibn Khaldoun, Tiaret, Algérie.*

[c]*Hassan First University of Settat, FST, Rayonnement-Matière et Instrumentation, S3M, 26000, Settat, Morocco*

[d]*Materials Science and Nano-engineering, Mohammed VI Polytechnic University Lot 660 Hay Moulay Rachid, Ben Guerir, Morocco*

[e]*Laboratoire de Cristallographie-Thermodynamique, Faculté de Chimie, Université des Sciences et de la Technologie Houari Boumediene, BP32, Al Alia, 16111, Algiers, Algeria*

Abstract

The structural and electrical properties of $NaBa_{(2-x)}Nd_{2x/3}Nb_5O_{15}$ ceramics were reported. All samples were prepared by the conventional solid-state reaction. A Room temperature X-ray study has allowed identifying the stabilization of tetragonal Tungsten Bronzes (TTB) structure with P4bm as space group for low Nd^{3+} concentration, whereas a centrosymmetric space group P4/mbm has been revealed for the high concentration. The dielectric study carried out on the prepared ceramics showed that the studied system undergo a behavior change from normal ferroelectric to a relaxor one with the increasing Neodymium amount. The complex impedance spectroscopy highlighted a thermally activated relaxation process in our samples. A short-range relaxation is proposed for x = 0.3 sample, while a possible coexistence of both localized and long-range relaxation for x = 1. Further, the Nyquist plot of the impedance is given for the low and higher Nd^{3+} samples and a simple model is proposed to fit the results.

Keywords: Tetragonal Tungsten Bronze; Crystal structure; Dielectric; Complex impedance spectroscopy; Raman spectroscopy.

* Corresponding author: abdel.ilah.lahmar@u-picardie.fr (A. Lahmar)

1. Introduction

Tetragonal tungsten bronze structural type (TTB), have been recognised of his potential applications in different fields like ferroelectricity [1- 4], ferroelasticity [5, 6] electro-optic [7], non-linear optic [8], elasto-optic [9], FRAM [10, 11] etc. The corresponding general crystal chemical formula of TTB is: $(A)_2(B)_4(C)_4(M)_8(M')_2O_{30}$, with M and M' cations forming octahedral cavities arranged in the manner to delimit wide tunnels running parallel to [001], with three type of sections (Figure 1): pentagonal (B), square (A), and trigonal (C).

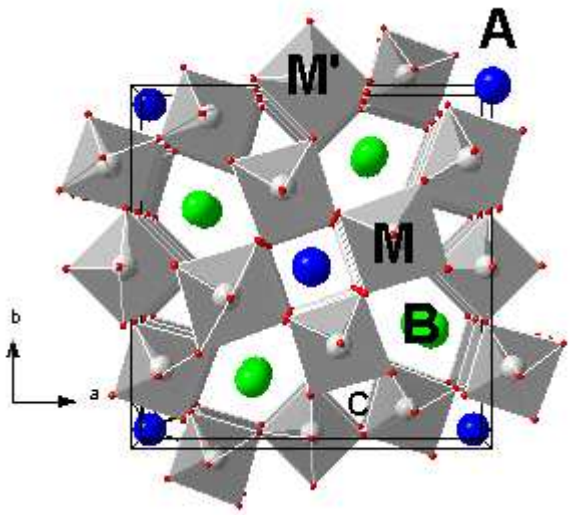

Figure.1: View of tetragonal tungsten bronze structure along [001].

It is interesting to mention that TTB structure is different to the most known perovskites [12-15]; complex perovskites [16, 17] or spinel structures [18-23]. In fact, TTB structure allows a wide variety of compensated substitutions depending on the size of cations, which should be located in the appropriate site of the lattice. Large size ions like K^+ cations are located in 15-fold co-ordinated cavities (B), medium size ions like Sr^{2+} cations will fill the 12-fold co-ordinated spheres (A) and very small size ions like Li^+ can rather easily enter the 9-fold cavities (C). However, the latter cavities are exceptionally occupied as in the case of $K_6Li_4Nb_{10}O_{30}$ [24]. Numerous works have reported that the physical properties characteristic of bronze-type phases can be modulated by appropriate ionic substitutions [25].

Especially, the mixed niobate of barium and sodium $Ba_2NaNb_5O_{15}$ (BNN) has been the subject of numerous physicochemical studies (stoichiometry, crystal growth, ferroelectric ferroelastic, electro-optic, etc.) due to its exceptional non-linear qualities promising as generator of a second harmonic of a laser beam at 0.53 µm [26].

In fact, BNN represents only one point of a solid solution, isolated within the ternary diagram Na_2O-BO-Nb_2O_5, with tetragonal tungsten bronze structure type [27]. Some authors have also noted a variation in stoichiometry in the vicinity of BNN and given formulations $Ba_{4+x}Na_{2-2x}Nb_{10}O_{30}$ (Jamieson et al) or $Ba_{4+x}Na_{2-2x}\square_xNb_{10}O_{30}$ (Singh et al.) with □ represents a cation deficiency in sodium sites [28, 29].

Noting that in this structure Ba^{2+} ions occupy the pentagonal tunnels, Na^+ ions occupy the square tunnels (and induce strong deformation there), while the triangular tunnel remains empty. For the octahedral lattice. The niobium ions Nb^{5+} are statistically distributed in the oxygen octahedra (see Figure.1).

Concerning the physical properties of this compound, BNN undergoes a phase transition from the paraelectric phase (space group P4/mbm) to the ferroelectric phase (space group P4bm) at Tc = 580 °C, for the stoichiometric composition where the lattice parameters are a = b = 12.45 Å and c = 3.98 Å [30]. However, this material does not keep the tetragonal symmetry up to room temperature; it presents a complicated sequence of phase transitions involving the ferroelectric and ferroelastic as illustrated by the following diagram [31]:

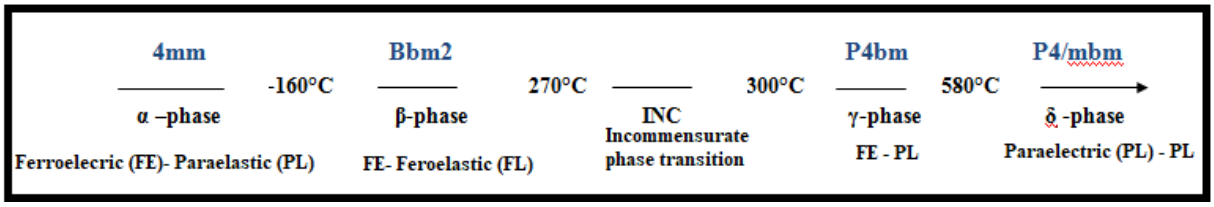

The existence of these undesirable INC transitions prevents the use of BNN in technological applications. Foulon et al. [32] find as a solution the incorporation of a small amount of the rare earth to supress the incommensurate phases. In our previous work [33], we confirm that the substitution of Na^+ by Nd^{3+} induces the stabilization of the tetragonal symmetry at room temperature with the suppression of the INC phase transition. However, as we mentioned above, Nd^{3+} is a medium size ion with ionic radii of r(Nd^{3+}) =1.27Å [34] compared to those of Na^+(1.39 Å) and Ba^{2+} (1.61 Å), thus it can be located in both Na^+ et Ba^{2+} sites with 15- and 12-fold coordination, respectively. For all these previous studies, a systematic analysis of how the site-location of Nd^{3+} affects the structure and subsequently the related physical properties is still lacking.

In the perspective of completing our previous work in order to have a whole picture on the real role of the incorporation of Nd in the BNN matrix, we are interested in the present paper to

study the substitution of Barium by Neodymium in the pentagonal sites. The emphasis is placed on how this substitution affects the structural and electrical properties of $Ba_2NaNb_5O_{15}$.

2. Experimental

Conventional solid-state reaction was used to elaborate the polycrystalline samples. Notice that other methods can be used of the preparation of oxide compounds [35-38]. The starting materials used herein were $BaCO_3$, Na_2CO_3 Nd_2O_3 and Nb_2O_5 (all from Sigma-Aldrich, USA) of high purity (>99.99%). The reagents were mixed and grounded in an agate mortar, with the respect of the adequate stoichiometry follows:

$$Na_2CO_3+2(2-x)BaCO_3 + \frac{2x}{3} Nd_2O_3+ 5Nb_2O_5 \rightarrow 2NaBa_{(2-x)}Nd_{(2x/3)}Nb_5O_{15}+(5-2x)CO_2$$

The starting mixture was thoroughly ground before to be submitted to various heat treatments from 300 up to 1250°C. A discover Brucker diffractometer (Cu Kα = 1.5406 Å) was used to check the phase purity and symmetry at room temperature. Room temperature Raman investigation was performed versus composition with a micro-Raman Renishaw spectrometer under an argon laser excitation under 20 mW for power. The microstructure of all ceramic has been obtained through Philips XL30 Field Emission Scanning Electron Microscope. Dielectric measurements were performed within the temperature range -100 to 600°C, using ceramic capacitors made of sintered disks with parallel faces painted with silver paste. Detailed information about the experimental procedure can be found elsewhere [33].

3. Results and Discussion

3.1. Microstructural analysis

The analysis of the micrographs presented in figure 2 allowed us to follow the microstructure of the studied ceramics to highlight the influence of the presence of Nd^{3+}. As shown in the figure, the phase corresponding to the composition x = 0.3 is formed mainly by grains of spherical shape. As the Nd^{3+} amount increases, a change in the shape as well as the size of the grains are observed. This is the case for x = 0.5 where we observed the appearance of square grains.

However, for x = 0.7, only square and rectangular shapes are observed, the microstructure is completely changed. In addition, a decrease in grain size, homogeneity of distribution, as well as very high density are observed. Noting that no notable change can be distinguished between the microstructures of x = 0.7 and that of x = 1. The radical change in the microstructure

observed from x = 0.7 suggests that a structural change may take place from this neodymium concentration.

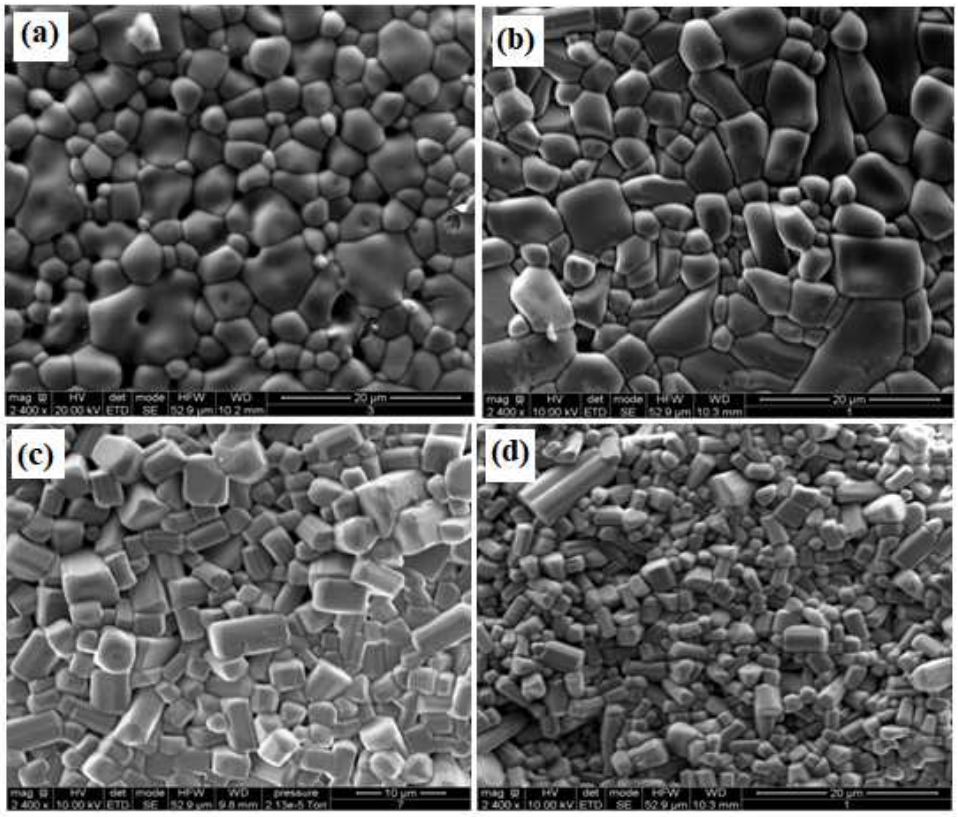

Figure.2. SEM micrographs of $Ba_2Na_{2-x}Nd_{2x/3}Nb_5O_{15}$ solid solution:

(a) x=0.3, (b) x=0.5,(c) x=0.7,(d) x=1

3.2. Crystal structure investigation

Figure 3(a) shows the X-ray powder diffraction patterns of $NaBa_{2-x}Nd_{2x/3}Nb_5O_{15}$ ($0 \leq x \leq 1$) compositions. Noting that a first indexation was performed for these compositions by means of the computer program Dicvol [39] in the tetragonal bronze type structure with non-Centro symmetric space group (*P4bm N° 100)*. However, a close look to the 2θ range between 29° and 34° (Figure 3 (b)) shows a noticeable shift in the positions of the reflections to the higher angles. This shift is linked to the substitution of the large cation Ba^{2+} by Nd^{3+} of smaller size [34]. Furthermore, when passing from the mother phase to x = 0.3 composition, a splitting of the reflections located in the vicinity of 29.70 ° and 32.25 °, respectively is observed. This behavior is due to the change from the orthorhombic (BNN) to tetragonal symmetry [32, 33].

However, no noticeable change could be detected with increasing Nd^{3+} content to x = 0.5. Albeit, the reflection observed around 30.40 ° (the left shoulder) disappears and the doubling

observed around 32.25 °, whose intensities seem comparable, turns into a large reflection with a shoulder on the left. The intensity of the first doubling peak become more pronounced (see fig.3 (b)). Thenceforth, this remarkable change observed in the shape of the peaks as well as the shift of the peaks with the increase in the rate of Nd^{3+}, led us to reconsider the indexing of the reflections, in particular for the compositions x = 0 , 7 and x = 1. A centrosymmetric space group suitable for the tetragonal tungsten bronze structure (P4 /mbm No. 127) was found to be more convenient. The crystalline parameters obtained after refinement of the structures are gathered together in table 1.

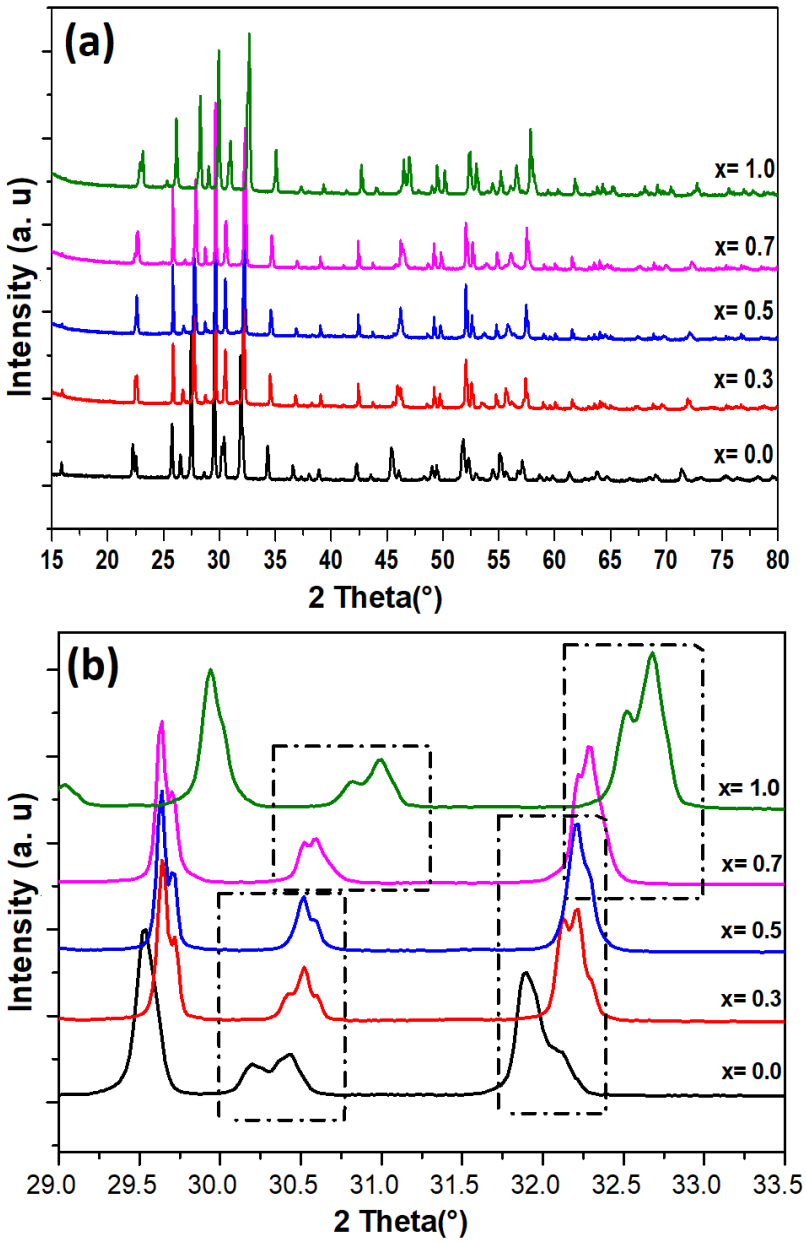

Figure.3. (a) X-ray diffraction patterns of the series $NaBa_{2-x}Nd_{2x/3}Nb_5O_{15}$ ($0 \leq x \leq 1$); (b) Illustration of the peaks evolution in the X-ray diffraction patterns of the series $NaBa_{2-x}Nd_{2x/3}Nb_5O_{15}$ ($0 \leq x \leq 1$) in the angular range of [29°, 34°].

Table 1. Details of Rietveld refinement conditions of the series $NaBa_{2-x}Nd_{2x/3}Nb_5O_{15}$ ($0.3 \leq x \leq 1$)

Composition	**x=0.3**	**x=0.5**	**x=0.7**	**x=1.0**
Symmetry	tetragonal	tetragonal	tetragonal	tetragonal
Space group	*P4bm*	*P4bm*	P4/*mbm*	P4/*mbm*
Z	2	2	2	2
Lattice parameters	a=b= 12.45341 (3) c= 3.96080 (1)	a=b= 12.46614(8) c= 3.90442 (2)	a=b= 12.45623 (3) c= 3.92243 (4)	a=b= 12.46636 (1) c= 3.90448 (1)
Volume	614.271 (2)	606.765 (8)	608.594 (2)	606.795 (7)
P-V function	0.76389 (5)	0.87389 (3)	0.95392 (2)	0.50657 (5)
Caglioti parameters	U= 0.09100 (3) V= -0.04101 (1) W= 0.01009 (2)	U= 0.11753 (2) V= -0.08328 (5) W= 0.02454 (1)	U= 0.08893 (2) V= -0.03877 (3) W= 0.00940 (8)	U= 0.08462 (2) V= -0.06361 (3) W= 0.02276 (5)
R_F/R_B	9.99 / 7.50	11.1 / 12.3	9.84/ 7.45	9.19 / 7.21
R_P/R_{wp}	5.21 / 7.35	4.73 / 6.58	6.18 / 9.14	4.44 / 6.32

The X-ray powder patterns were fitted to the calculated ones using a full-profile analysis program (FullProf) [40, 41]. The refinement of the powder XRD patterns were carried out with tetragonal (*P4bm*) for the compositions x=0, x=0.3 and x=0.5. In this case, the Nb^{5+} cations occupy 8d(x, y, z) and 2b(0, 0.5, z) sites and $Ba^{2+}/Na^{+}/Nd^{3+}$ cations are placed at 4c (x, x+1/2, z), while Na^{+}/Ba^{2+} are located in 2a (0, 0, z) sites. Finally, the oxygen atoms occupy the 8d Wyckoff positions (x, y, z), 4c(x, x+1/2, z) and 2b(0, 0.5, z). The compositions x= 0.7 and 1 were fitted with the tetragonal (P4/*mbm*). In this model Nb^{5+} atoms are located in 8j(x, y, 0.5) and 2c(0, 0.5, 0.5) sites. Ba^{2+}, Na^{+}, and Nd^{3+} are located in both crystallographic sites 4g(x, x+0.5, 0) and 2a(0, 0, 0). The oxygen atoms occupy the 8i, 8j, 4h, and 2d Wyckoff positions with the general positions 8i(x, y,0), 8j(x,y,0.5), 4h(x, x+0.5,0.5) and 2d(0, 0.5, 0). As an example, in figure 4 we show the typical Rietveld refinement patterns along with the difference plot, at room temperature, for $NaBa_{1.7}Nd_{0.2}Nb_5O_{15}$, $NaBa_{1.3}Nd_{0.467}Nb_5O_{15}$, and $NaBaNd_{0.667}Nb_5O_{15}$. It is worthy to note that significantly good residuals of the refinements are obtained. As an example, the refined structural parameters are given in table 2 for the compositions $NaBa_{1.7}Nd_{0.2}Nb_5O_{15}$ with *P4bm* as space group, and $NaBaNd_{0.667}Nb_5O_{15}$ with P4/mbm as space group.

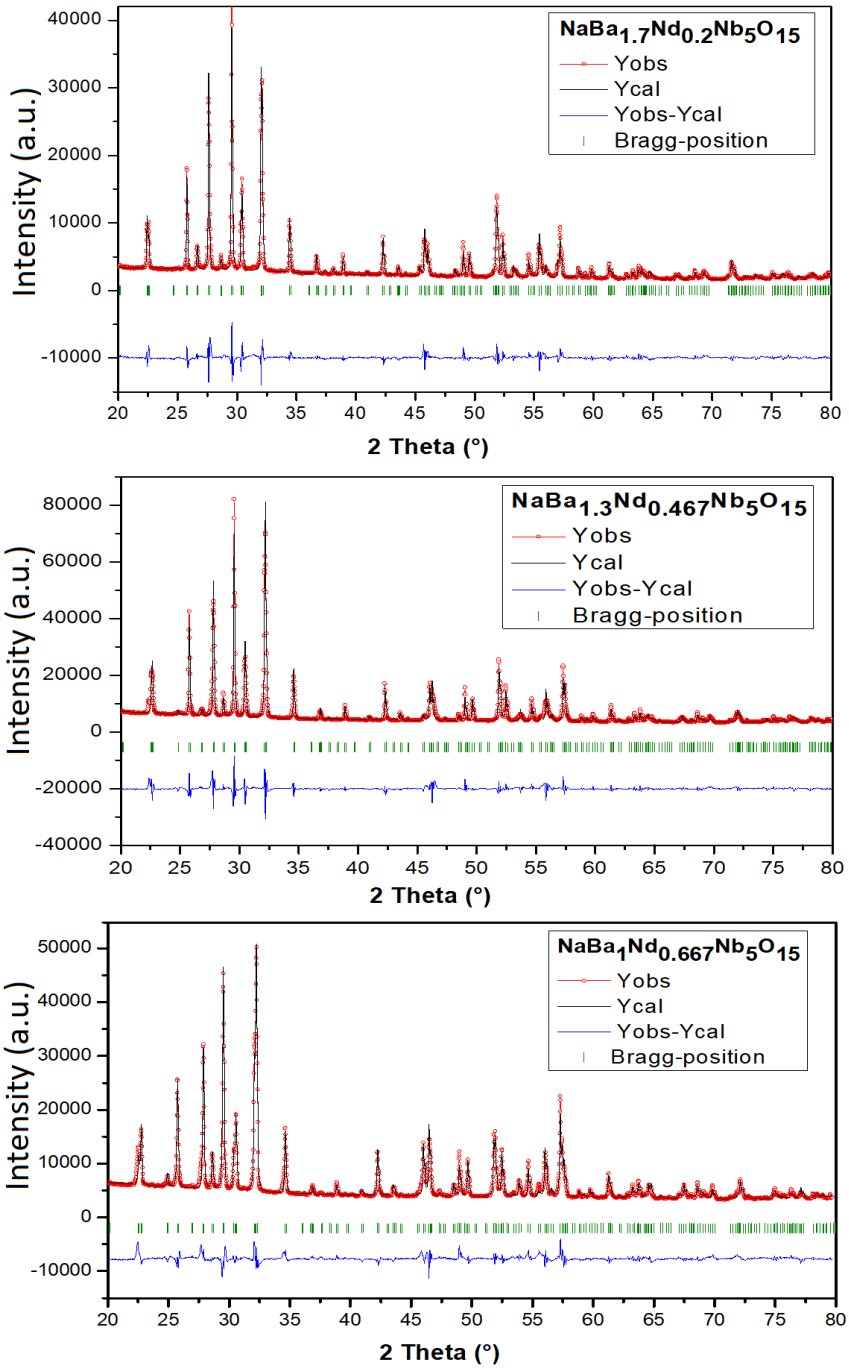

Figure.4. Plot of Rietveld refinement of the series $NaBa_{2-x}Nd_{2x/3}Nb_5O_{15}$ (x= 0.3, 0.7 and 1.0). The upper symbols illustrate the observed data (red circles) and the calculated pattern (solid line). The vertical markers show calculated positions of Bragg reflections. The lower curve is the difference diagram.

Table 2. Refined structural parameters for the composition *x*=0.3 with *P*4*bm* as space group and *x*=1.0 with P4/*mbm* as space group.

	Site	x	y	z	Biso	Occupancy
x= 0.3	**$NaBa_{1.7}Nd_{0.2}Nb_5O_{15}$** *(P4bm)*					
Ba/Nd/Na	4c	0.1716(3)	0.6716(3)	0.4380(2)	0.0571(5)	1.332/0.200/0.742
Ba/Na	2a	0.000	0.0000	0.5049(4)	0.5392(5)	0.368/0.258
Nb1	8d	0.07420(4)	0.2097(1)	-0.0605(6)	0.6863(2)	4
Nb2	2b	0.000	0.5000	-0.0722(6)	0.6863(2)	1
O1	8d	0.0035(3)	0.6562(6)	-0.1066(2)	1.6236(6)	4
O2	8d	0.0689(5)	0.8474(4)	0.8188(3)	1.6236(6)	4
O3	8d	0.0758(3)	0.2012(7)	0.3364(6)	1.6236(6)	4
O4	4c	0.2826(1)	0.7826(3)	-0.0176(4)	1.6236(6)	2
O5	2b	0.0000	0.5000	0.5116(2)	1.6236(6)	1
x= 1	**$NaBaNd_{0.667}Nb_5O_{15}$** (*P4/mbm*)					
Ba/Nd/Na	4g	0.1729(6)	0.6729(6)	0.0000	0.2391(3)	0.395/0.666/ 0.605
Na/Nd/Na	2a	0.0000	0.0000	0.0000	0.6393(2)	0.604/0.001/ 0.395
Nb1	8j	0.0753(2)	0.2118(3)	0.5000	0.4391(4)	4
Nb2	2c	0	0.5	0.5000	0.4391(4)	1
O1	8i	0.0588(5)	0.1834(5)	0.000	1.6873(5)	4
O2	8j	0.3383(2)	0.0083(6)	0.5000	1.6873(5)	4
O3	8j	0.1511(3)	0.0723(6)	0.5000	1.6873(5)	4
O4	4h	0.2853(4)	0.7853(4)	0.5000	1.6873(5)	2
O5	2d	0.0000	0.5000	0.0000	1.6873(5)	1

3.3. Raman spectroscopy analysis at room temperature

Recall that XRD analysis has allowed distinguishing two space groups for the studied system. The compositions x = 0.3 and x = 0.5 crystallize in the non-centrosymmetric P4bm, while x = 0.7 and x = 1 adopt a centrosymmetric space group *P4/mbm*. The irreducible representation associated with both space groups are given by Eq.1 [42] and Eq.2 [43] respectively:

$\Gamma(vibr) = 19A_1+14B_1+18B_2+35E$ for P4bm (Eq. 1)

$\Gamma(vibr) = 12A_{1g}+6A_{1u}+10A_{2g}+12A_{2u}+10B_{1g}+12B_{2g}+5B_{2u}+14E_g+28E_u$ for P4/mbm (Eq. 2)

With A_{1g}, B_{1g}, B_{2g} and E_g are active Raman modes (48 modes) while A_{2u} and E_u are infrared active modes (38 optical modes).

Experimentally, the number of modes observed is much smaller than what expected theoretically, signature of a structural disorder resulting in the overlap of different Raman modes. As evidenced from the figure 5, there are three dominant vibration bands (ν_1), (ν_2), and (ν_3) characteristic of the vibrations within the octahedra $[NbO_6]^{7-}$ [44- 47]. Further, a group of low intensity modes are observed at low wavenumber (denoted ν_0 in this work)

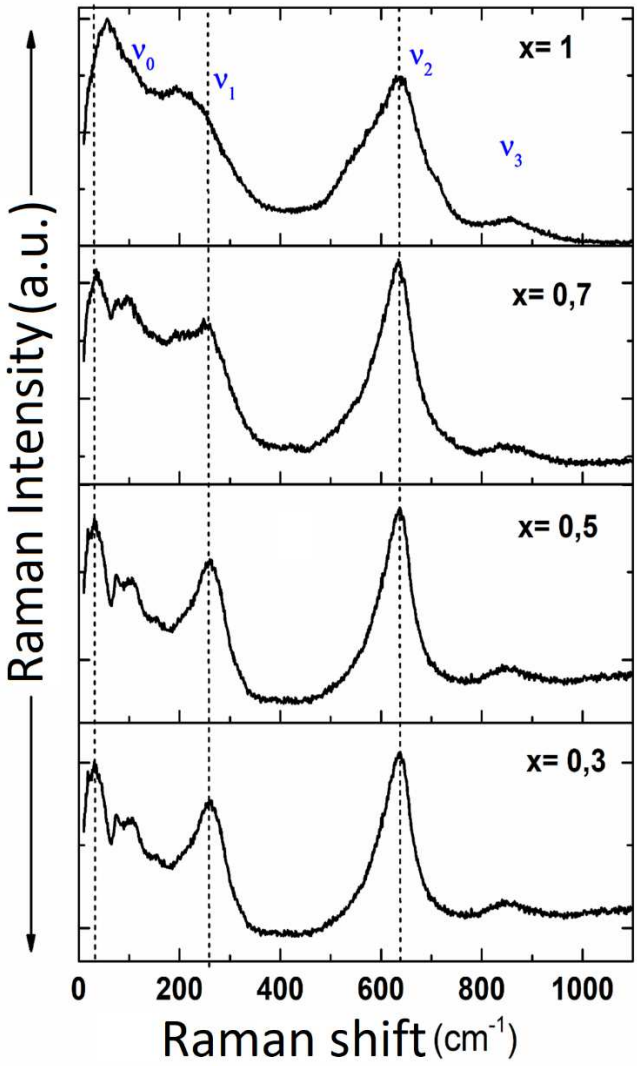

Figure.5. Room temperature Raman spectra of Na $Ba_{(2-x)}Nd_{2x/3}Nb_5O_{15}$ (x = 0,3, 0,5, 0,7and 1) compositions.

From the comparison, it seems that there is no noticeable change between the recorded spectra, which shows a similar shape to that obtained generally for disordered TTB structure [48, 33]. However, a close look to the low wavenumber region [10 cm^{-1}- 300 cm^{-1}], some changes could

be spotted from x = 0.7. In fact, υ_1 mode shows a slight shift in its position with the appearance of a new shoulder to its left. Further, the mode splitting observed around 100 cm^{-1}, seems to merge in a single band. In addition, there is a reversal of the intensities between ν_1 and ν_0 (the doublet). This reversal of intensities is detectable from the composition x = 0.7. These transformations become more visible when the concentration of Nd^{3+} increases (x=1).

These changes are related to in crystal symmetry change evidenced by the structural study.

3.4. Dielectric investigations

The dielectric measurements as a function of the temperature were carried out for different compositions of the solid solution $Ba_{(2-x)}Nd_{(2x/3)}NaNb_5O_{15}$ at three frequencies 10, 100 and 1000 kHz as shown in figure 6. The examination of these graphs shows that for the composition x = 0.3 the phase transition is located near 280 ° C. No clear relaxation behavior could be depicted form the plots, the behavior is that of a classical ferroelectric (Fig. 6 (a)).

Figure 6 (b) shows the evolution of the constant and the dielectric losses of the composition x = 0.5. As it can be seen from the plots, two dielectric anomalies are visible. The first one is located in the positive range of temperature around 120 °C, which seems to be frequency independent. However, the second one is manifested by a maximum located towards lower temperatures in the range 20°C-50°C and it is frequency dependent. It is likely that this composition exhibits two types of behavior: a classical ferroelectric one, as in the case for x = 0.3 and more likely a relaxor behavior.

The further increase of the neodymium content (x = 0.7 and x= 1) shows that only one single broad peak is observed, with the maximum (T_m) is frequency dependent. This behavior is characteristic of ferroelectric relaxor materials (Fig. 6 (c) and 6(d)). These results are in good agreement with the room temperature structural investigations where x = 0.3 and x = 0.5 are crystallized in non-centrosymmetric compatible with classical ferroelectric material (observation of a transition in the positive temperature range). Whereas, a centrosymmetric space group (P4/mbm) is obtained for x = 0.7 and x = 0.1; that corroborates the absence of transitions above room temperature.

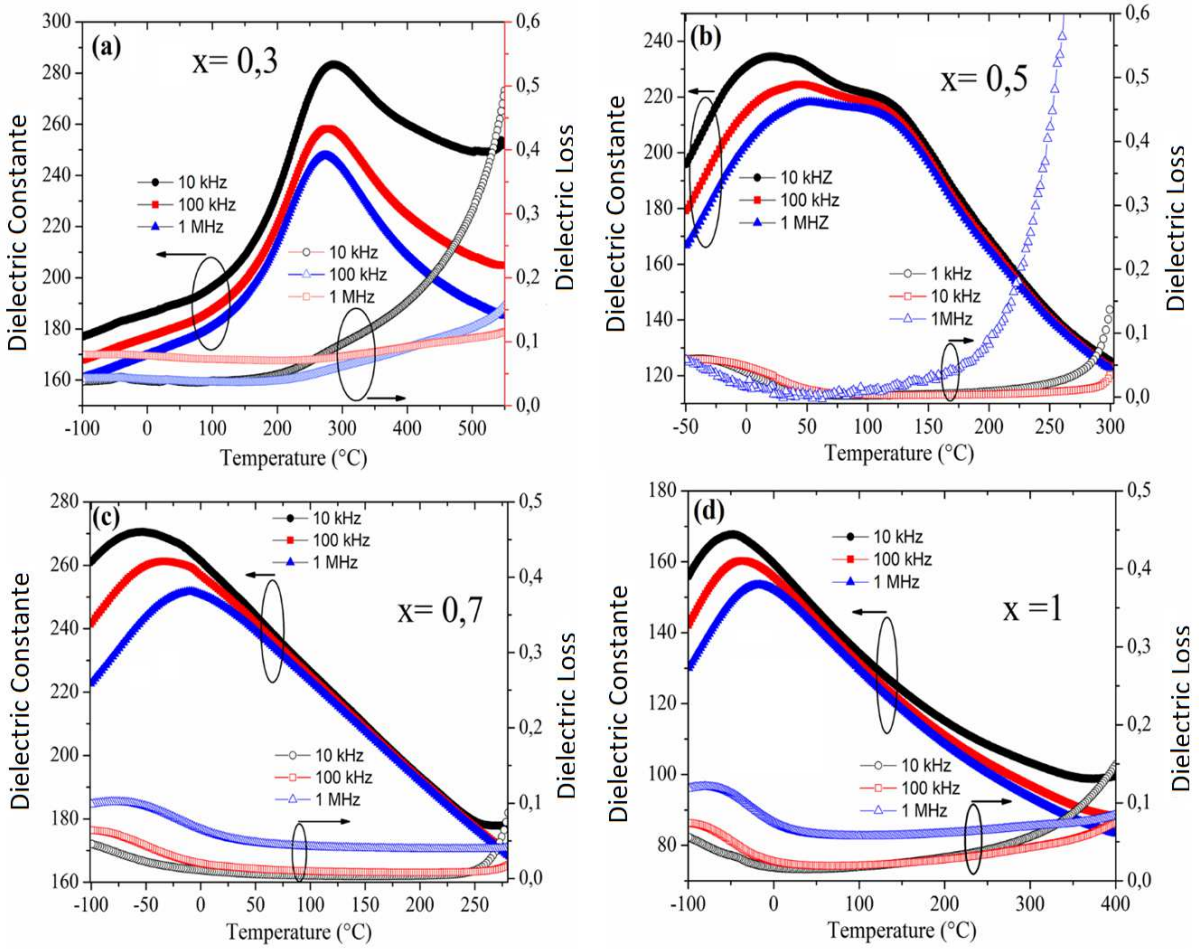

Figure.6 Temperature dependence of the dielectric constant and dielectric loss of (a) x = 0.3; (b) x = 0.5; (c) x = 0.7 and (d) x = 1.

3.5. Complex impedance spectroscopy of $NaBa_{(2-x)}Na_{(2x/3)}Nb_5O_{15}$ ceramics

It is well known that in polycrystalline materials the microstructure plays an important role in the transport properties of the system. Therefore, a detailed impedance study may give us a proper relation between the electrical properties of our material and their microstructure [49]. Figure 7 (a-d) presents the frequency dependent real and imaginary part of the impedance at various temperature (440°C to 550°C) for the $NaBa_{(2-x)}Na_{(2x/3)}Nb_5O_{15}$ ceramics (x = 0.3 and 1). It can be noted from the figures that Z″(f) curve present a maximum (figure 7 (b, d)), whereas a decrease can be observed in Z′(f) plot (figure 7 (a, c)). This last behavior reveals the occurrence of a relaxation within the studied materials, which might be assigned to space charges. Regarding Z″(f) curves, we can observe that the relaxation frequency for both compounds is temperature dependent with an evident shift towards high frequencies. This behavior reveals a thermally activated relaxation process in our samples [50].

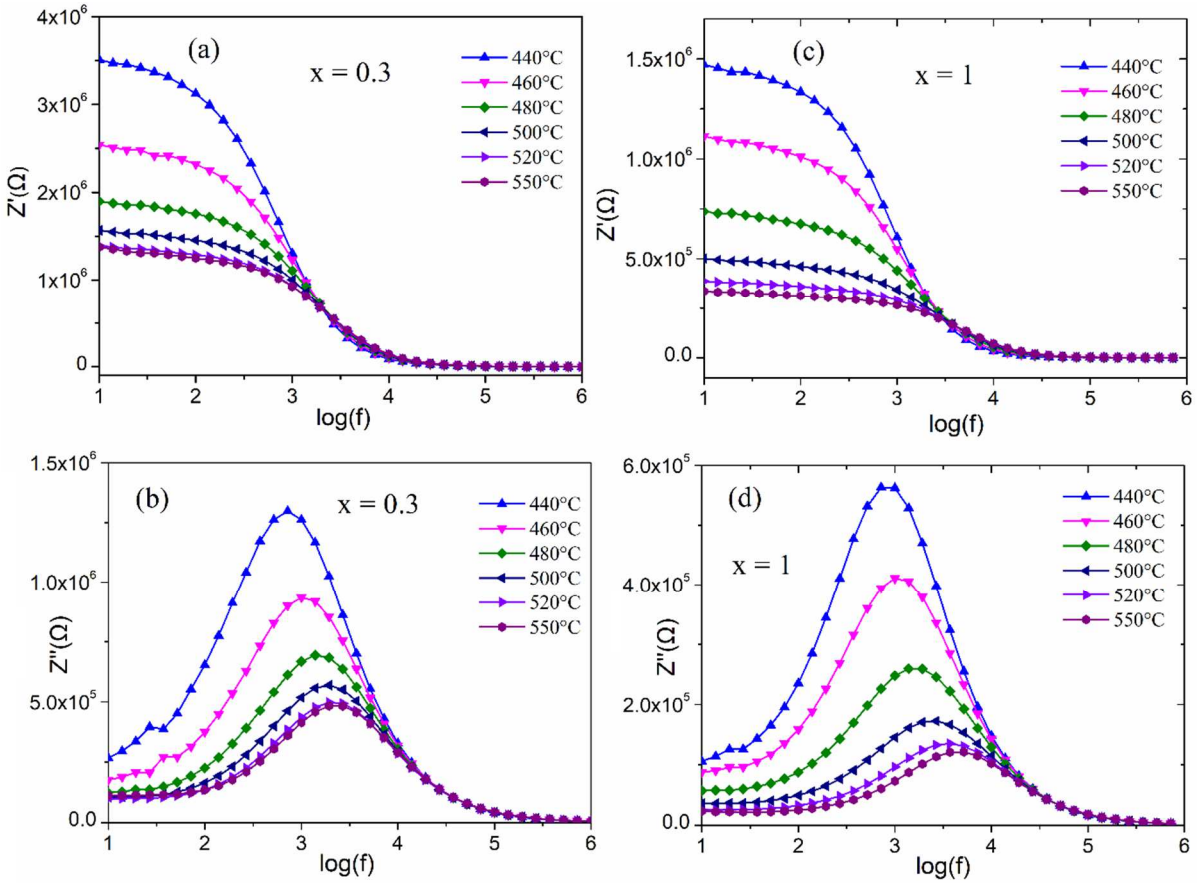

Figure.7. Real impedance Z′(f) curves for (a) x = 0.3, and for (c) x = 1. Imaginary impedance Z″(f) curves for (b) x = 0.3, and (d) for x = 1.

Besides, in the high frequencies, a merging is noticed for all temperatures, which is due to the release of space charges owing to the reduction in the barrier properties of the samples. In addition, we can observe that the relaxation frequency for both samples is different, where the composition x = 1 presents a relaxation at higher frequency compared to x = 0.3.

The exploitation of the complex electric modulus (M*) along with the complex impedance formalism may give an important information about our samples. Since it is well known that Z″(f) represents the resistive properties of the material, whereas M″(f) reveals the localized relaxation process [51]. Therefore, we present in figure 8 (a-d) the real and imaginary part of the electric modulus as a function of frequency and at different temperatures for the $NaBa_{(2-x)}Na_{(2x/3)}Nb_5O_{15}$ ceramics (x = 0.3 and 1). The plotted curves also reveal a temperature-dependent relaxation frequency in the material with a peak maximum in M″(f), and an increase in M′(f). The study of the electric modulus generally reveals the existence of the grains and/or grain boundaries contributions in the system. In our case, the appearance of one peak in M″(f) plot indicates the sole contribution of grains in our samples.

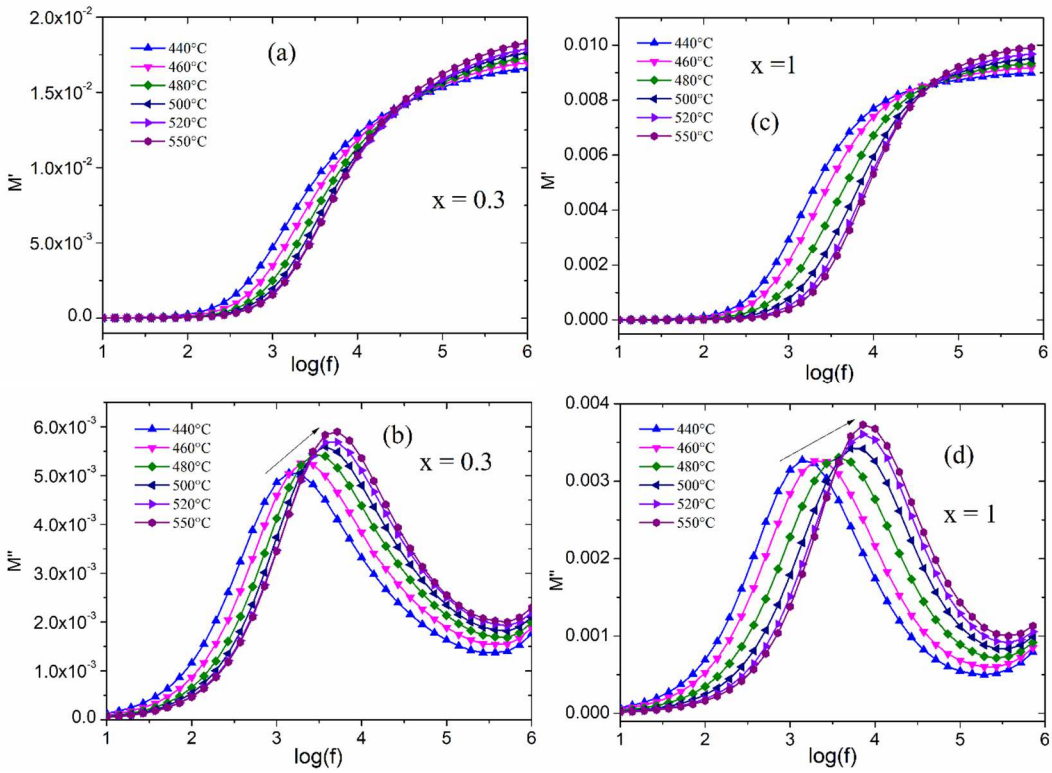

Figure.8. Real part of the electric modulus M′(f) as a function of frequency for (a) x = 0.3, and (c) x = 1. Imaginary part of the electric modulus M″(f) as a function of frequency for (b) x = 0.3 and (d) x = 1.

Figure 9 (a, b) presents a comparison of the imaginary part of the electric modulus and the impedance at 550°C. The combined curves can give information about the relaxation mechanism occurring in our samples. Notice that the overlapping of M″ and Z″ curves is an indication of the delocalized relaxation [52]. In our samples, we can observe a difference in the peak positions of the curves which is more pronounced for x = 0.3 than for x = 1. We suggest that for x = 0.3 sample, a short-range relaxation is occurring, while a possible coexistence of both localized and long-range relaxation coexist for x = 1 sample.

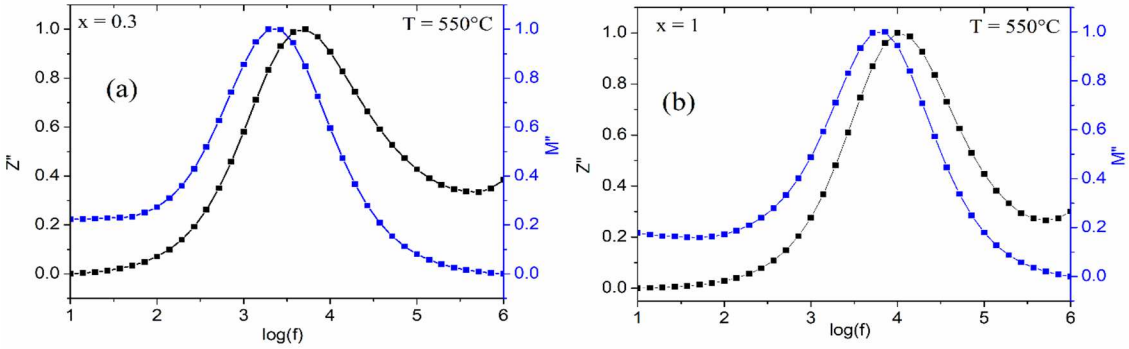

Figure.9.: Comparison of the Z″(f) and M″(f) curves for (a) x = 0.3 and (b) for x = 1 samples, at 550°C.

To extract more information about the resistive properties of our samples, we plotted in figure 10 (a-c) the Nyquist plots (Cole-Cole) of the impedance formalism for both samples at different temperatures. The plots point out well-resolved semi-circles for all the studied temperatures. It can be observed that the radius of the semi-circles is decreasing as the temperature increases, which demonstrates the semiconducting nature of our samples. Besides, using a model (inset of figure 10 (c)), we could fit the obtained experimental Nyquist plots. Our proposed model contains the grain contribution, i.e., grain resistance and capacitance (R, C). In addition, the absence of the overlapping peak positions of the imaginary impedance and electric modulus in figure10 denotes the departure from an ideal behavior and implies the use of a constant phase element (CPE) in the circuit [53]. Figure 10(c) presents a comparison of the fitted Nyquist plots for both samples at 550°C. Our model seems to fit well the experimental data. Table 3 regroups the electrical parameters used for the fit for all the studied temperatures. We observe that the resistance of both compounds is decreasing as the temperature increases. This behavior is demonstrating the Negative Temperature Coefficient of Resistivity (NTCR) of our samples. A similar trend is observed for the capacitance. Besides, the resistance decreases as the value of *x* increases, such that for 550°C, a significant different can be observed in the resistance of the samples ($R = 1.31\times10^{6}$ for x = 0.3, and $R = 3.20\times10^{5}$ for x = 1).

Table 3: Resistance and Capacitance parameters resulting from the fit of the $NaBa_{(2-x)}Na_{(2x/3)}Nb_5O_{15}$ ceramics (x = 0.3 and 1) at 550°C.

	x = 0.3		x = 1	
	R (ohm)	C (F)	R (ohm)	C (F)
T = 440°C	3.60×10^{6}	3.42×10^{-11}	1.49×10^{6}	6.30×10^{-11}
T = 460°C	2.56×10^{6}	3.35×10^{-11}	1.16×10^{6}	6.25×10^{-11}
T = 480°C	1.88×10^{6}	3.16×10^{-11}	7.54×10^{5}	6.02×10^{-11}
T = 500°C	1.55×10^{6}	3.12×10^{-11}	5.04×10^{5}	5.83×10^{-11}
T = 520°C	1.36×10^{6}	3.04×10^{-11}	3.80×10^{5}	5.39×10^{-11}
T = 550°C	1.31×10^{6}	2.84×10^{-11}	3.20×10^{5}	5.25×10^{-11}

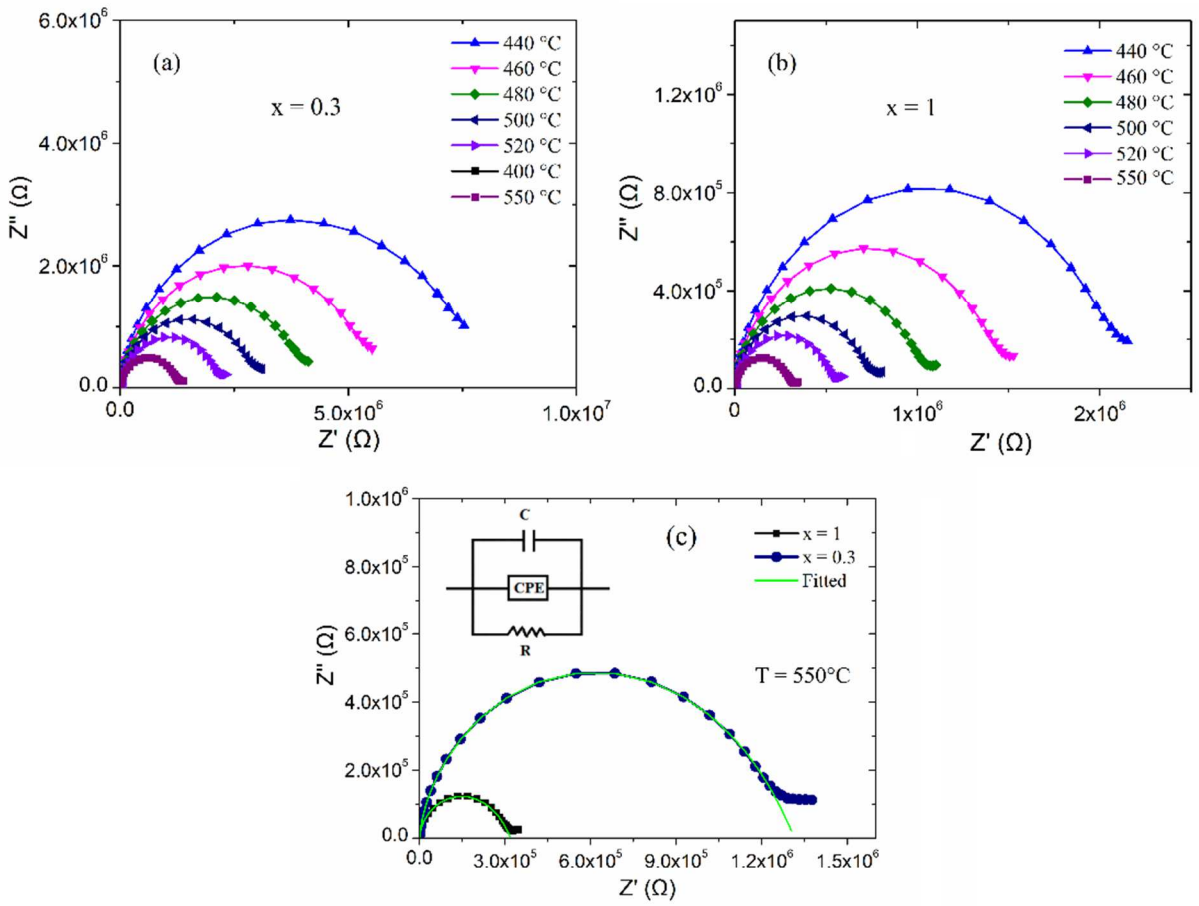

Figure 10. Cole-Cole plots of (a) x = 0.3, (b) x = 1 at different temperatures, and (c) a comparison of x = 0.3 and x = 1 at 550°C. The inset present the model used to fit our systems.

Figure 11 (a, b) presents the frequency dependence of the ac electrical conductivity (σ_{ac}) at different temperatures. The latter was calculated using the following relation $\sigma_{ac} = \varepsilon_0\varepsilon_r\tan\delta$. We can observe from the figures a plateau in the low frequency region, whereas at high frequencies no conductivity dispersion can be noted. We can thus conclude about the occurrence of a transition from long-range hopping to short-range ionic motion in the samples.

To get more information from the conductivity plots of our samples, we performed fitting of the ac conductivity using the Jonscher power law described as follow (e.g. inset of figure 11) [54]:

$$\sigma_{ac} = \sigma_{dc} + A_1\omega^{S_1} \qquad \text{(Eq. 3)}$$

Where S_1 take values between 0 and 1, and σ_{dc} is dc conductivity of the samples. Table 4, present the fitting parameters for different temperatures (from 400°C to 550°C). We can note that the conductivity of both samples is increasing as the temperature increases. This behavior is related to the thermal activated process. Figure 12 (a, b) shows the logarithmic scale of the

ac and dc conductivity versus 1000/T for the two samples. The plots are observed to be linear and follow the following Arrhenius equation [55]:

$$\sigma = \sigma_0 \exp\left(-\frac{E_a}{K_B T}\right) \quad \text{(Eq. 4)}$$

Where the activation energy is E_a, the Boltzmann constant K_B, and the pre-exponential factor σ_0. The activation energies extracted from both ac and dc conductivity plots are illustrated in figure 12.

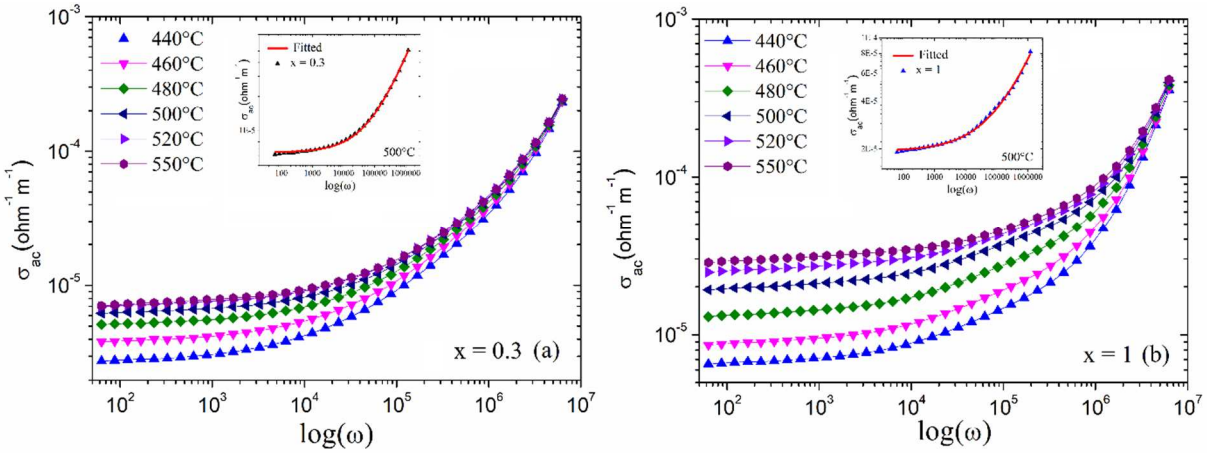

Figure.11. Conductivity as a function of frequency and temperature for (a) x = 0.3; (b) x = 1. Insets show an example of the fitted plots at 500°C (using the Jonscher Power Law).

Table 4: Jonscher Power Law fitting parameters for different temperatures for x = 0.3 and x = 1 samples.

$NaBa_{(2-x)}Nd_{2x/3}Nb_5O_{15}$ (x = 0.3)								
	400	420	440	460	480	500	520	550
σ_{dc}	1E-6	1.97E-6	2.93E-6	4.01E-6	5.34E-6	6.47E-6	7.32E-6	7.56E-6
A_1	3.57E-10	1.12E-9	1.63E-9	1.81E-9	2.15E-9	2.41E-9	2.58E-9	2.35E-9
S_1	0.797	0.731	0.713	0.712	0.704	0.704	0.697	0.701
$NaBa_{(2-x)}Nd_{2x/3}Nb_5O_{15}$ (x = 1)								
	400	420	440	460	480	500	520	550
σ_{dc}	5.066E-6	5.86E-6	7.10E-6	9.19E-6	1.29E-5	1.94E-5	2.53E-5	2.97E-5
A_1	5.48E-9	5.73E-9	2.44E-9	6.04E-9	4.11E-8	4.43E-8	4.06E-8	2.10E-8
S_1	0.593	0.596	0.687	0.634	0.506	0.514	0.524	0.574

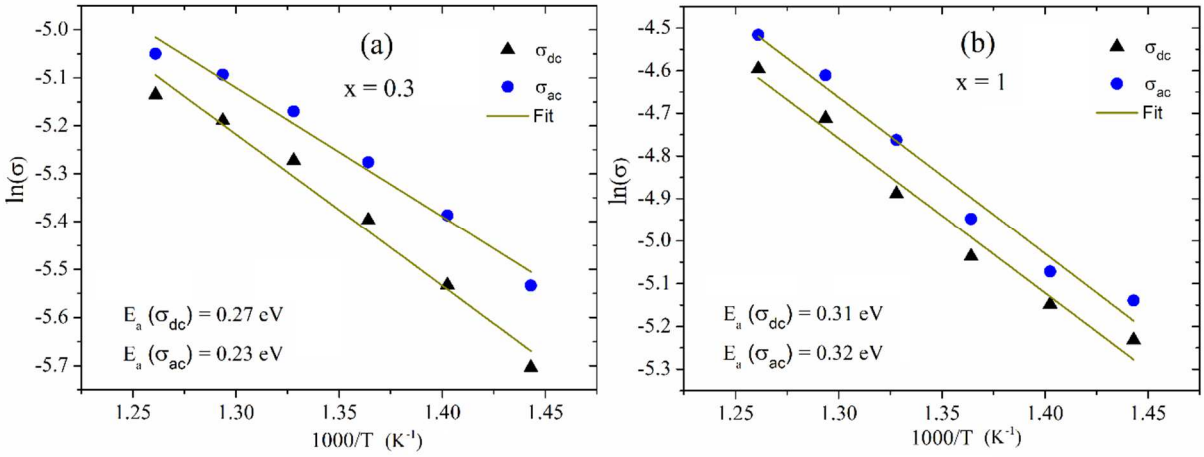

Figure.12. Arrhenius plots of $NaBa_{(2-x)}Nd_{2x/3}Nb_5O_{15}$ samples with (a) x = 0.3, and (b) x = 1. The activation energies extracted from the dc and ac conductivity for each sample are given in the plots.

It is reported that if the parameter S_1 is temperature dependent, many-body interactions among charge carriers and defect states could be expected [56]. In our case, the value of S_1 is not temperature dependent (Table 4), indicating that the conduction process should be unique. Furthermore, the close values of the activation energies of the dc and the ac conductivities reveals the existence of a similar potential barriers for local hopping (ac) and long-range movement (dc) and that energy barrier heights are randomly distributed [57]. Recall that in $Ba_2NaNb_5O_{15}$ vacancies constitute a part of the structure. Further, this phase is delimited by non-stoichiometric $Ba_{1.90}Na_{1.2}Nb_5O_{15}$ and $Ba_{2.27}Na_{0.46}Nb_5O_{15}$ compositions [33]. Differently to the perovskite with fully-occupied A sites, in the TTB-type compound (like BNN) the large free space created by the large Ba^{2+} cations (A sites) is favor of oxygen ion migration. Such cationic vacancies may be responsible for the obtained lower activation energy; in agreement with what it is reported by Hongqiang Ma et al. in $BaBiNb_5O_{15}$ with TTB structure type [58].

4. Conclusion

Compositions of $NaBa_{(2-x)}Nd_{2x/3}Nb_5O_{15}$ ($0 \leq x \leq 1$) solid solution were prepared using the conventional reaction method. Microstructural investigations revealed a change in the shape and in the size of the grains with the increase of Nd^{3+} concentration. X-ray diffraction study has confirmed that the whole range of composition is of tetragonal tungsten bronze structural type. Compositions with low Neodymium concentration revealed a normal ferroelectric behavior, which changed to relaxor one for Nd- high concentration samples.

The CIS study revealed a thermally activated relaxation process in our samples. Besides, a short-range relaxation is suggested for x = 0.3 sample, whereas for x = 1, a possible coexistence of both localized and long-range relaxation is occurring. Further, a simple model was proposed to fit the Nyquist plot of the impedance data of the low and higher Nd^{3+} samples. The determination of activation energy of both ac and dc conductivities revealed close values indicating that the conduction mechanism is unique and can be attributed to the migration of oxygen ion governed by A-sites vacancies.

Acknowledgements

The authors gratefully acknowledge the financial support of the "Program Hubert Curien" (PHC-Tassili No. 18MDU107/39978VH) and the European Union's Horizon 2020 research and innovation program ENGIMA.

References

[1] Magnéli, A. (1949) The Crystal Structure of Tetragonal Potassium Tungsten Bronze. Arkiv fr Kemi, 1, 213-221. Scientific Research Publishing.

[2] M.E. Lines, A.M. Glass, Principles and Applications of Ferroelectrics and Related Materials, Principles and Applications of Ferroelectrics and Related Materials. (2010). https://doi.org/10.1093/ACPROF:OSO/9780198507789.001.0001.

[3] V.S. FILIP'EV, YA.E. CHERNER, Z. v BONDARENKO, E.G. FESENKO, Transformations de phase dans les ferroélectriques A2Pb4Nb10O30 ayant une structure du type bronze de tungstène quadratique, Fizika Tverdogo Tela. 28 (1986) 1338–1343.

[4] B.N. Savenka, B. Sangaa and F. Proket, Ferroelectrics 107 (1990) 207.

[5] M.J. Ravez, A. Perron-Simon, B. Elouadi, L. Rivoallan, P. Hagenmuller, Evolution de quelques proprietes physiques de phases de structure "bronzes de tungstene quadratiques" par remplacement de l'element Alcalino-Terreux par le plomb, Journal of Physics and Chemistry of Solids. 37 (1976) 949–952. https://doi.org/https://doi.org/10.1016/0022-3697(76)90036-6.

[6] J. Ravez, B. Elouadi, Couplage ferroelastique-ferroelectrique dans les phases de structure "bronzes de tungstene quadratiques," Materials Research Bulletin. 10 (1975) 1249–1254. https://doi.org/https://doi.org/10.1016/0025-5408(75)90035-5.

[7] P.V. Nenzo, E.G. Sencer and A.A. Balman, J. Appl. Phys. Lett. 11(1971) 23.

[8] S.C. Abrahams, P.B. Jamieson, J.L. Bernstein, Ferroelectric Tungsten Bronze-Type Crystal Structures. III. Potassium Lithium Niobate K(6−x−y)Li(4+x)Nb(10+y)O30, The Journal of Chemical Physics. 54 (1971) 2355–2364. https://doi.org/10.1063/1.1675186.

[9] A.M. Glass, Investigation of the Electrical Properties of Sr1−xBaxNb2O6 with Special Reference to Pyroelectric Detection, Journal of Applied Physics. 40 (1969) 4699–4713. https://doi.org/10.1063/1.1657277.

[10] N. Wakiya, J.-K. Wang, A. Saiki, K. Shinozaki, N. Mizutani, Synthesis and dielectric properties of Ba1−xR2x/3Nb2O6 (R: rare earth) with tetragonal tungsten bronze structure, Journal of the European Ceramic Society. 19 (1999) 1071–1075. https://doi.org/https://doi.org/10.1016/S0955-2219(98)00376-8.

[11] H.F. Cheng, G.S. Chiou, K.S. Liu, I.N. Lin, Ferroelectric properties of (Sr0.5Ba0.5)Nb2O6 thin films synthesized by pulsed laser deposition, Applied Surface Science. 113–114 (1997) 217–221. https://doi.org/10.1016/S0169-4332(96)00794-5.

[12] S. v Trukhanov, A. v Trukhanov, V.G. Kostishin, L. v Panina, I.S. Kazakevich, V.A. Turchenko, V. v Oleinik, E.S. Yakovenko, L.Yu. Matsui, Magnetic and absorbing properties of M-type substituted hexaferrites BaFe12–

xGaxO19 (0.1 < x < 1.2), Journal of Experimental and Theoretical Physics. 123 (2016) 461–469. https://doi.org/10.1134/S1063776116090089.
[13] D.A. Vinnik, A.Yu. Starikov, V.E. Zhivulin, K.A. Astapovich, V.A. Turchenko, T.I. Zubar, S. v Trukhanov, J. Kohout, T. Kmječ, O. Yakovenko, L. Matzui, A.S.B. Sombra, D. Zhou, R.B. Jotania, C. Singh, Y. Yang, A. v Trukhanov, Changes in the Structure, Magnetization, and Resistivity of BaFe12–xTixO19, ACS Applied Electronic Materials. 3 (2021) 1583–1593. https://doi.org/10.1021/acsaelm.0c01081.
[14] S. v Trukhanov, T.I. Zubar, V.A. Turchenko, An.V. Trukhanov, T. Kmječ, J. Kohout, L. Matzui, O. Yakovenko, D.A. Vinnik, A.Yu. Starikov, V.E. Zhivulin, A.S.B. Sombra, D. Zhou, R.B. Jotania, C. Singh, A. v Trukhanov, Exploration of crystal structure, magnetic and dielectric properties of titanium-barium hexaferrites, Materials Science and Engineering: B. 272 (2021) 115345. https://doi.org/https://doi.org/10.1016/j.mseb.2021.115345.
[15] S. v. Trukhanov, I.O. Troyanchuk, N. v. Pushkarev, H. Szymczak, Magnetic properties of anion-deficient La1−x BaxMnO3−x/2 (0≤x≤0.30) manganites, Journal of Experimental and Theoretical Physics 2003 96:1. 96 (2003) 110–117. https://doi.org/10.1134/1.1545390.
[16] H.H. Guo, D. Zhou, C. Du, P.J. Wang, W.F. Liu, L.X. Pang, Q.P. Wang, J.Z. Su, C. Singh, S. Trukhanov, Temperature stable Li2Ti0.75(Mg1/3Nb2/3)0.25O3-based microwave dielectric ceramics with low sintering temperature and ultra-low dielectric loss for dielectric resonator antenna applications, Journal of Materials Chemistry C. 8 (2020) 4690–4700. https://doi.org/10.1039/D0TC00326C.
[17] S.Z. Hao, D. Zhou, F. Hussain, W.F. Liu, J.Z. Su, D.W. Wang, Q.P. Wang, Z.M. Qi, C. Singh, S. Trukhanov, Structure, spectral analysis and microwave dielectric properties of novel x(NaBi)0.5MoO4-(1-x)Bi2/3MoO4 (x = 0.2 ~ 0.8) ceramics with low sintering temperatures, Journal of the European Ceramic Society. 40 (2020) 3569–3576. https://doi.org/10.1016/J.JEURCERAMSOC.2020.03.074.
[18] A. Manohar, K. Chintagumpala, K.H. Kim, Mixed Zn–Ni spinel ferrites: Structure, magnetic hyperthermia and photocatalytic properties, Ceramics International. 47 (2021) 7052–7061. https://doi.org/10.1016/J.CERAMINT.2020.11.056.
[19] A. Manohar, C. Krishnamoorthi, K.C.B. Naidu, B.P. Narasaiah, Dielectric, Magnetic Hyperthermia and Photocatalytic Properties of Mg.Zn.FeO Nanocrystals, IEEE Transactions on Magnetics. 56 (2020). https://doi.org/10.1109/TMAG.2020.3024717.
[20] A. Manohar, V. Vijayakanth, M.R. Pallavolu, K.H. Kim, Effects of Ni - substitution on structural, magnetic hyperthermia, photocatalytic and cytotoxicity study of MgFe2O4 nanoparticles, Journal of Alloys and Compounds. 879 (2021) 160515. https://doi.org/10.1016/J.JALLCOM.2021.160515.
[21] A. v. Trukhanov, K.A. Astapovich, V.A. Turchenko, M.A. Almessiere, Y. Slimani, A. Baykal, A.S.B. Sombra, D. Zhou, R.B. Jotania, C. Singh, T.I. Zubar, D.I. Tishkevich, S. v. Trukhanov, Influence of the dysprosium ions on structure, magnetic characteristics and origin of the reflection losses in the Ni–Co spinels, Journal of Alloys and Compounds. 841 (2020) 155667. https://doi.org/10.1016/J.JALLCOM.2020.155667.
[22] M. v. Zdorovets, A.L. Kozlovskiy, D.I. Shlimas, D.B. Borgekov, Phase transformations in FeCo – Fe2CoO4/Co3O4-spinel nanostructures as a result of thermal annealing and their practical application, Journal of Materials Science: Materials in Electronics. 32 (2021) 16694–16705. https://doi.org/10.1007/S10854-021-06226-5/FIGURES/6.
[23] A. Manohar, C. Krishnamoorthi, Synthesis and magnetic hyperthermia studies on high susceptible Fe1−xMgxFe2O4 superparamagnetic nanospheres, Journal of Magnetism and Magnetic Materials. 443 (2017) 267–274. https://doi.org/10.1016/J.JMMM.2017.07.065.
[24] J. Ravez, A. Perron-Simon, P. Hagenmuller, Les phases de structure “bronzes de tungstèn quadratiques” : règles cristallochimiques, relations entre propriétés ferroélectriques et distorsions structurales, Annales de Chimie. 1 (1976) 251–268. https://hal.archives-ouvertes.fr/hal-00131554 (accessed November 27, 2021).
[25] F.W. Ainger, J.A. Beswick, W.P. Bickley, R. Clarke, G. v. Smith, Ferroelectrics in the lithium potassium niobate system, Http://Dx.Doi.Org/10.1080/00150197108241506. 2 (2011) 183–199. https://doi.org/10.1080/00150197108241506.
[26] J.E. Geusic, H.J. Levinstein, J.J. Rubin, S. Singh, L.G. van Uitert, THE NONLINEAR OPTICAL PROPERTIES OF Ba2NaNb5O15, Applied Physics Letters. 11 (2004) 269. https://doi.org/10.1063/1.1755129.
[27] J-M Reau, B. Elouadi, J. Ravez, P. Hagenmuller, Influence de la Substitution Tungstène-Niobium sur les Propriétés Cristallographiques et Diélectriques de la Solution Solide de Compositions Limites $Ba_{2.5-x}Na_{2x}Nb_5O_{15}$

(0,23≤ x≤0,60). Le Système $BaNb_2O_6$-$(NaNbO_3)2$-$(WO_3)_2$ à 1050°C, J. Solid State Chem. 15 (1975) 18. https://doi.org/10.1016/0022-4596(75)90266-2.
[28] P.B. Jamieson, S.C. Abrahams, J.L. Bernstein, Ferroelectric Tungsten Bronze-Type Crystal Structures. II. Barium Sodium Niobate Ba(4 + x)Na(2 − 2x)Nb10O30, The Journal of Chemical Physics. 50 (2003) 4352. https://doi.org/10.1063/1.1670903.
[29] S. Singh, D.A. Draegert, J.E. Geusic, Optical and Ferroelectric Properties of Barium Sodium Niobate, Physical Review B. 2 (1970) 2709. https://doi.org/10.1103/PhysRevB.2.2709. [30] R.L. Barns, IUCr, Barium sodium niobate (Ba(4+x)Na(2−2x)Nb10O30): crystallographic data and thermal expansion coefficients, Urn:Issn:0021-8898. 1 (1968) 290–292. https://doi.org/10.1107/S0021889868005522.
[31] J. Schneck, J. Primot, R. von der Mühll, J. Ravez, New phase transition with increasing symmetry on cooling in barium sodium niobate, Solid State Communications. 21 (1977) 57–60. https://doi.org/10.1016/0038-1098(77)91478-8.
[32] G. Foulon, M. Ferriol, A. Brenier, M.T. Cohen-Adad, M. Boudeulle, G. Boulon, Nonlinear single-crystal fibers of undoped or Nd3+-doped niobates: growth by LHPG, spectroscopy and second harmonic generation, Optical Materials. 8 (1997) 65–74. https://doi.org/10.1016/S0925-3467(97)00027-X.
[33] M. Belarbi, Y. Tamraoui, B. Manoun, A. Cantaluppi, Y. Gagou, K. Taibi, M. el Marssi, A. Lahmar, Structural, dielectric and energy storage properties of Neodymium niobate with tetragonal tungsten bronze structure, Physica B: Condensed Matter. 618 (2021) 413185. https://doi.org/10.1016/J.PHYSB.2021.413185.
[34] R.D. Shannon, IUCr, Revised effective ionic radii and systematic studies of interatomic distances in halides and chalcogenides, Urn:Issn:0567-7394. 32 (1976) 751–767. https://doi.org/10.1107/S0567739476001551.
[35] A. Manohar, C. Krishnamoorthi, C. Pavithra, N. Thota, Magnetic Hyperthermia and Photocatalytic Properties of MnFe2O4 Nanoparticles Synthesized by Solvothermal Reflux Method, Journal of Superconductivity and Novel Magnetism. 34 (2021) 251–259. https://doi.org/10.1007/S10948-020-05685-X/FIGURES/10.
[36] A. Manohar, C. Krishnamoorthi, Structural, optical, dielectric and magnetic properties of CaFe2O4 nanocrystals prepared by solvothermal reflux method, Journal of Alloys and Compounds. 722 (2017) 818–827. https://doi.org/10.1016/J.JALLCOM.2017.06.145.
[37] A. Thakur, N. Sharma, M. Bhatti, M. Sharma, A. v. Trukhanov, S. v. Trukhanov, L. v. Panina, K.A. Astapovich, P. Thakur, Synthesis of barium ferrite nanoparticles using rhizome extract of Acorus Calamus: Characterization and its efficacy against different plant phytopathogenic fungi, Nano-Structures & Nano-Objects. 24 (2020) 100599. https://doi.org/10.1016/J.NANOSO.2020.100599.
[38] H. Cheema, S. Kumar, P.A. Alvi, B.L. Choudhary, U. Kumar, Synthesis and physical properties of nanopowder and electrical properties of bulk samples of ZnFe2-xNixO4 (x: 0, 0.05, 0.10), Advanced Powder Technology. 31 (2020) 4241–4252. https://doi.org/10.1016/J.APT.2020.09.001.
[39] A. Boultif, D. Loueer, Indexing of powder diffraction patterns for low-symmetry lattices by the successive dichotomy method, Urn:Issn:0021-8898. 24 (1991) 987–993. https://doi.org/10.1107/S0021889891006441.
[40] J. Rodriguez-Carvajal, FULLPROF 2000: A Rietveld Refinement and Pattern Matching Analysis Program, 2008.
[41] T. Roisnel, T. Roisnel, J. Rodríguez-carvajal, WinPLOTR: a Windows tool for powder diffraction analysis, IN MATERIALS SCIENCE FORUM. PROCEEDINGS OF THE EUROPEAN POWDER DIFFRACTION CONF. (EPDIC 7. (2001). http://citeseerx.ist.psu.edu/viewdoc/summary?doi=10.1.1.561.2063 (2021).
[42] M. Bouziane, M. Taibi, L. Saviot, A. Boukhari, Raman characterization of Pb2Na1−xLaxNb5−xFexO15 and Pb0.5(5−x)LaxNb5−xFexO15 (0≤x≤1) solid solutions, Physica B: Condensed Matter. 406 (2011) 4257–4260. https://doi.org/10.1016/J.PHYSB.2011.08.025.
[43] V. Hornebecq, C. Elissalde, V. Porokhonskyy, V. Bovtun, J. Petzelt, I. Gregora, M. Maglione, J. Ravez, Dielectric relaxation in tetragonal tungsten bronze ceramics, Journal of Physics and Chemistry of Solids. 64 (2003) 471–476. https://doi.org/10.1016/S0022-3697(02)00342-6.
[44] R. Clarke, D. Siapkas, Temperature-dependent Raman spectra of ferroelectric potassium strontium niobate, Journal of Physics C: Solid State Physics. 8 (1975) 377. https://doi.org/10.1088/0022-3719/8/3/016.
[45] G. Burns, J.D. Axe, D.F. O'Kane, Raman measurements of NaBa2Nb5O15 and related ferroelectrics, Solid State Communications. 7 (1969) 933–936. https://doi.org/10.1016/0038-1098(69)90545-6.
[46] H. Xia, H. Yu, H. Yang, K. Wang, B. Zhao, Raman and infrared reflectivity spectra of potassium lithium niobate single crystals, Physical Review B. 55 (1997) 14892. https://doi.org/10.1103/PhysRevB.55.14892.

[47] H.-R. Xia, L.-X. Li, H. Yu, X.-L. Meng, L. Zhu, L.-J. Hu, Raman and Infrared Spectra of Nd-Doped Barium Sodium Niobate Crystals, Crystal Research and Technology. 34 (1999) 901–910. https://doi.org/https://doi.org/10.1002/(SICI)1521-4079(199908)34:7<901::AID-CRAT901>3.0.CO;2-F.
[48] A. Lahmar, S. Ganschow, J. Doerschel, K. Tsuzuku, M. Couzi, B. Elouadi, Crystal Growth and Dielectric Study of the Niobate Series K3Sr2RNb10O30 (R = Lanthanide) of Tungsten Bronze Structure, Eurasian Chemico-Technological Journal. 11 (2009) 1–6. https://doi.org/10.18321/ECTJ407.
[49] D.K. Pradhan, R.N.P. Choudhary, C. Rinaldi, R.S. Katiyar, Effect of Mn substitution on electrical and magnetic properties of Bi0.9La0.1FeO3, Journal of Applied Physics. 106 (2009) 024102. https://doi.org/10.1063/1.3158121.
[50] E. Axelrod, A. Givant, J. Shappir, Y. Feldman, A. Sa'ar, Dielectric relaxation and transport in porous silicon, Physical Review B. 65 (2002) 165429. https://doi.org/10.1103/PhysRevB.65.165429.
[51] J. Liu, C.G. Duan, W.G. Yin, W.N. Mei, R.W. Smith, J.R. Hardy, Large dielectric constant and Maxwell-Wagner relaxation in Bi 2/3Cu3Ti4O12, Physical Review B - Condensed Matter and Materials Physics. 70 (2004) 144106. https://doi.org/10.1103/PHYSREVB.70.144106/FIGURES/11/MEDIUM.
[52] M. Coşkun, A.O. Polat, F.M. Coşkun, Z. Durmuş, C.M. Caglar, A. Türüt, The electrical modulus and other dielectric properties by the impedance spectroscopy of LaCrO 3 and LaCr 0.90 Ir 0.10 O 3 perovskites, RSC Advances. 8 (2018) 4634–4648. https://doi.org/10.1039/C7RA13261A.
[53] M. Benyoussef, M. Zannen, J. Belhadi, B. Manoun, J.L. Dellis, A. Lahmar, M. el Marssi, Complex impedance and Raman spectroscopy of Na0.5(Bi1-xDyx)0.5TiO3 ceramics, Ceramics International. 46 (2020) 10979–10991. https://doi.org/10.1016/J.CERAMINT.2020.01.114.
[54] A.K. Jonscher, The 'universal' dielectric response, Nature 1977 267:5613. 267 (1977) 673–679. https://doi.org/10.1038/267673a0.
[55] S. Lanfredi, J.F. Carvalho, A.C. Hernandes, Electric and dielectric properties of Bi12TiO20 single crystals, Journal of Applied Physics. 88 (2000) 283. https://doi.org/10.1063/1.373654.
[56] X. Chen, Y. Wang, J. Chen, H. Zhou, L. Fang, L. Liu, Dielectric Properties and Impedance Analysis of K0.5Na0.5NbO3–Ba2NaNb5O15 Ceramics with Good Dielectric Temperature Stability, Journal of the American Ceramic Society. 96 (2013) 3489–3493. https://doi.org/10.1111/JACE.12514.
[57] C.H. Song, H.W. Choi, M. Kim, G.Y. Jin, Y.S. Yang, Electrical Relaxations of Amorphous xKNbO3-(1-x)SiO2 (x = 0.33, 0.5, 0.67, 0.8), JKPS. 51 (2007) 674. https://doi.org/10.3938/JKPS.51.674.
[58] H. Ma, K. Lin, L. Liu, B. Yang, Y. Rong, J. Chen, J. Deng, S. Kawaguchi, K. Kato, X. Xing, Structure and electrical properties of tetragonal tungsten bronze Ba 2 CeFeNb 4 O 15, RSC Advances. 5 (2015) 76957–76962. https://doi.org/10.1039/C5RA16115K.